



ELSEVIER

Atmospheric Research 53 (2000) 91–116

ATMOSPHERIC  
RESEARCH

www.elsevier.com/locate/atmos

# The effects of giant cloud condensation nuclei on the development of precipitation in convective clouds — a numerical study

Yan Yin, Zev Levin<sup>\*</sup>, Tamir G. Reisin, Shalva Tzivion

*Department of Geophysics and Planetary Sciences, Raymond and Beverly Sackler, Faculty of Exact Sciences, Tel Aviv University, P.O. Box 39040, Ramat Aviv 69978, Israel*

---

## Abstract

Numerical experiments are conducted to investigate the effects of giant cloud condensation nuclei (CCN) on the development of precipitation in mixed-phase convective clouds. The results show that the strongest effects of introducing giant CCN occur when the background concentration of small nuclei is high, as that in continental clouds. Under these conditions, the coalescence between water drops is enhanced due to the inclusion of giant CCN, resulting in an early development of large drops at the lower parts of the clouds. It also leads to the formation of larger graupel particles and to more intensive radar reflectivities. When the background concentration of small nuclei is low, as in maritime clouds, the effect of the giant CCN is smaller and the development of precipitation is dominated by the droplets formed on large nuclei. © 2000 Elsevier Science B.V. All rights reserved.

*Keywords:* Giant CCN; Convective cloud; Numerical modeling

---

## 1. Introduction

Cloud condensation nuclei (CCN) are the centers on which cloud droplets can form. These particles range in diameter from about 0.06  $\mu\text{m}$  to greater than 2  $\mu\text{m}$ . This wide range of sizes has traditionally been subdivided into three classes (e.g., Pruppacher and Klett, 1978): small or Aitken nuclei ( $\sim 0.06\text{--}0.2 \mu\text{m}$ ), large (0.2–2  $\mu\text{m}$ ) and giant ( $> 2 \mu\text{m}$ ). Since small CCN are the most numerous in the atmosphere, they effectively

---

<sup>\*</sup> Corresponding author. Fax: +972-3-6408274.

*E-mail address:* zev@hail.tau.ac.il (Z. Levin).

determine the total concentration of droplets in a cloud. The concentrations of the small CCN can be measured with thermal gradient diffusion cloud chambers (e.g., Twomey, 1963; Radke and Turner, 1972; Hudson and Squires, 1976). Although less numerous than the small CCN and much more difficult to measure, large and giant CCN provide the centers upon which larger cloud droplets can form. Under certain conditions these larger drops can lead to rapid formation of raindrop embryos.

The role of giant CCN in the initiation of warm rain had been commonly accepted for a long time until Woodcock et al. (1971) cast doubt on this old belief. Woodcock et al. observed the iodine–chlorine ratio of particles ranging in size from small nuclei to raindrops sampled in Hawaii and found that the I/Cl ratio in raindrops is of the same order as that in small nuclei ( $10^{-12}$ – $10^{-14}$  g), but differs by one order from the ratio in giant nuclei. They concluded that in warm oceanic tradewind clouds, giant salt nuclei might not be essential to the formation of raindrops. Takahashi (1976) reached similar conclusions by numerical simulation of warm rain development in a maritime cloud. In addition, Takahashi and Lee (1978) concluded on the basis of their improved numerical model, that nuclei of mass less than  $10^{-15}$  g are efficient for the initiation of warm rain and that the mass distribution of nuclei usually observed around Hawaii is the optimum distribution of nuclei for warm rain development. All of these studies are related to rain development from warm marine clouds in which the CCN concentrations are usually less than  $100 \text{ cm}^{-3}$ .

Johnson (1982) investigated the role of giant and ultragiant ( $> 10 \text{ }\mu\text{m}$  in radius) aerosol particles in warm rain initiation. His results showed that when ingested in growing clouds, these particles produce a tail of large drops in the cloud-droplet distribution. The effects of these large drops are more important for continental than for maritime clouds. Similar conclusions were also drawn by Kuba and Takeda (1983).

From the above studies one can conclude that giant CCN have little influence on the warm rain development in maritime clouds. On the other hand, the effect of such giant CCN on continental clouds could be significant. In addition, we have little knowledge about how giant CCN influence the rain formation in mixed phase clouds, especially the effects of the giant CCN on the development of the ice phase precipitation particles. Many measurements (e.g., Eagan et al., 1974; Hindman et al., 1977; Mather, 1991) show that the precipitation development from convective clouds has been affected by the emission from paper mills. Mather (1991) stated that it is the addition of the “long tail” produced by the paper mill to the cloud-base droplet spectra that is apparently turning on, or at least enhancing, coalescence in affected storms. Numerical experiments by Reisin et al. (1996a) showed that the precipitation from mixed convective clouds are to a larger extent, dependent on the warm microphysical processes, and that the CCN concentration and the distributions of initial droplets are the main factors determining the precipitation. It is, therefore, important to study the influences of giant CCN on the development of precipitation in cold convective clouds.

In this study, numerical simulations were conducted in an attempt to shed some light on the above-mentioned problems. The model used was a two-dimensional slab-symmetric nonhydrostatic cloud model with detailed treatment of both the warm and the cold microphysical processes. Special efforts were paid to the investigation of the contributions of giant CCN on the development of precipitation particles and radar reflectivity.

To simulate the development of precipitation particles from nuclei, the microphysical processes, especially the CCN nucleation process, needed to be treated accurately. Different approaches have been used to deal with the CCN nucleation process (e.g., Mordy, 1959; Arnason and Greenfield, 1972; Fitzgerald, 1974; Takahashi, 1976; Kuba and Takeda, 1983; Flossmann et al., 1985; Kogan, 1991). In this work, a CCN nucleation scheme based on Kogan (1991) has been adopted. All the microphysical processes were solved using the multi-moments method (Tzivion et al., 1987, 1989; Feingold et al., 1988; Reisin et al., 1996b). This method provides a solution of the kinetic transfer equations that conserves the balance between two or more physical moments in each spectral bin of the cloud particles' distribution function.

In the following section a brief description of the numerical model is given. The initial conditions used in this study and a description of the numerical experiments is given in Section 3. The results of the numerical experiments are presented in Section 4. The discussion and conclusions follow in Section 5.

## 2. The cloud model

### 2.1. The dynamic model

The dynamic framework was a two-dimensional slab-symmetric nonhydrostatic cloud model. The wind components in the horizontal and vertical directions were calculated based on the vorticity equation and stream function. The dynamic equations were also solved for the virtual potential temperature perturbation ( $\theta_v$ ), the specific humidity perturbation ( $q$ ), the concentration of CCN, the number and mass concentrations for each type of cloud particles considered (For details see Appendix A).

### 2.2. The microphysical model

The present model was designed to simulate the evolution of precipitation particles in mixed-phase cloud starting from cloud nuclei. The warm microphysical processes included were nucleation of CCN, condensation and evaporation, collision-coalescence, and binary breakup. The ice microphysical processes included were drop freezing, ice nucleation (deposition and condensation-freezing, and contact nucleation), ice multiplication, deposition and sublimation of ice, interactions of ice–ice and ice–drop (aggregation, accretion and riming), melting of ice particles, and sedimentation of both drops and ice particles. All the microphysical processes had been formulated using kinetic equations and solved using the method of multi-moments. Three different ice species were considered: ice crystals, graupel particles, and snowflakes (aggregates of ice crystals). Each type of particles was divided into 34 bins with mass doubling in each bin ( $x_{k+1} = 2x_k$ ,  $k = 1, 34$ ). The masses at the beginning of the first bin and the end of last bin for both liquid and solid phases were  $0.1598 \times 10^{-13}$  and  $0.17468 \times 10^{-3}$  kg, which correspond to drop diameters of 3.125 and 8063  $\mu\text{m}$ , respectively.

The temporal changes in the particles size distribution function  $n(m, x, z, t)$  with respect to mass  $m$ , at location  $(x, z)$  and time  $t$ , due to the microphysical processes can be generally expressed as:

$$\begin{aligned} \frac{\delta n_y(m, x, z, t)}{\delta t} = & \left( \frac{\delta n_y(m, x, z, t)}{\delta t} \right)_{\text{nucl}} + \left( \frac{\delta n_y(m, x, z, t)}{\delta t} \right)_{\text{cond/evap, depos/sublim}} \\ & + \left( \frac{\delta n_y(m, x, z, t)}{\delta t} \right)_{\text{coll/breakup, ice interac}} + \left( \frac{\delta n_y(m, x, z, t)}{\delta t} \right)_{\text{sedim}} \\ & + \left( \frac{\delta n_y(m, x, z, t)}{\delta t} \right)_{\text{freezing}} + \left( \frac{\delta n_y(m, x, z, t)}{\delta t} \right)_{\text{melting}}, \end{aligned} \quad (1)$$

where  $n_y(m, x, z, t)$  is the size distribution function of the species  $y$ : water drops, ice crystals, graupel particles, or snowflakes.

To obtain a set of moment equations for each bin for each species, the operator  $\int_{x_k}^{x_{k+1}} m^j dm$  was applied to both sides of Eq. 1. In the present study we solved for the first two moments of the category distribution function,  $N_{y_k}$  and  $M_{y_k}$ , the number and mass concentrations of species  $y$  in the  $k$ th bin, respectively:

$$N_{y_k}(t) = \int_{x_k}^{x_{k+1}} n_{y_k}(m, t) dm, \quad (2)$$

$$M_{y_k}(t) = \int_{x_k}^{x_{k+1}} m n_{y_k}(m, t) dm. \quad (3)$$

Here  $y$  has the same meaning as above. The dependence on  $x, z$  is implicit in the above equations. As Tzivion et al. (1987) showed, the distribution function,  $n_{y_k}$ , needs to be prescribed only when the integration is over an incomplete category interval. In such cases, the distribution function is approximated using a linear function, positive within the category.

The radar reflectivity factor of species  $y$  in bin  $k$  is calculated using the nondimensional parameter  $\bar{\xi}$  that relates different moments (for details see Tzivion et al., 1989):

$$Z_{y_k}(t) = \left[ \frac{6}{\rho\pi} \right]^2 \int_{x_k}^{x_{k+1}} x^2 n(x) dx = \bar{\xi} \left[ \frac{6}{\rho\pi} \right]^2 \frac{M_k^2(t)}{N_k(t)}, \quad (4)$$

and the total reflectivity factor is given by

$$Z(t) = \sum_{y=w,i,g,sk=1}^{K_{\max}} Z_{y_k}(t). \quad (5)$$

The radar reflectivity factor in dBZ is  $10\log Z$  with  $Z$  in  $\text{mm}^6 \text{m}^{-3}$ . It should be noted that the radar reflectivity defined here is valid only for Rayleigh-approximation of the scattering coefficient and for spherical precipitation particles. For large hailstones and nonspherical particles, the scattering process will deviate from Rayleigh scattering behavior.

The effective radius of hydrometers at a certain point  $(x, z)$  and time  $t$  was calculated using the first two moments as:

$$r_{\text{eff}}(x, z, t) = \frac{\int_0^\infty r^3 n(r) dr}{\int_0^\infty r^2 n(r) dr} = \left( \frac{3}{4\pi\rho} \right)^{\frac{1}{3}} \frac{\sum_{k=1}^{K_{\text{max}}} M_k(x, z, t)}{\sum_{k=1}^{K_{\text{max}}} \xi_{2/3} M_k(x, z, t)^{\frac{2}{3}} N_k(x, z, t)^{\frac{1}{3}}} \quad (6)$$

where,  $\xi_{2/3}$  is a nondimensional parameter that relates noninteger moments [see Tzivion et al. (1989) for details].

Except for the CCN nucleation process, which has been improved and will be discussed in detail here, all the other processes were based on previous studies (e.g., Tzivion et al., 1994; Reisin et al., 1996b) and will only be briefly described here. We refer the interested readers to the above-mentioned papers for details.

### 2.2.1. Nucleation of drops

At each spatial point, the CCN of a certain size were activated when the supersaturation calculated by the model exceeded the critical value determined by the Köhler equation (Pruppacher and Klett, 1997):

$$S = \frac{A}{r} - \frac{B r^3}{r^3}, \quad (7)$$

where,

$$A = \frac{2\sigma}{\rho_w R_v T}, \quad B = \frac{\nu\Phi_s \epsilon M_w \rho_N}{M_N \rho_w}, \quad (8)$$

in which,  $\nu$  is the number of ions that results from the dissociation of a salt molecule in water. For NaCl,  $\nu = 2$ , and for  $(\text{NH}_4)_2\text{SO}_4$ ,  $\nu = 3$ .  $\sigma$  is the surface tension of the solution drop.  $\epsilon$  is the fraction of water-soluble material of an aerosol particle.  $M_N$  and  $M_w$  are the molecular weights of CCN and water, respectively.  $\Phi_s$  is osmotic coefficient for the aqueous solution.  $\rho_N$  and  $\rho_w$  are the densities of CCN and water, respectively.

Cloud condensation nuclei begin to grow by absorption of water vapor long before they enter the cloud. These wetted particles provide the initial sizes for subsequent condensational growth. The main problem is how to include these wetted particles in the model calculations. In previous cloud models, different schemes were often adopted to calculate the size of these initial wet particles. Mordy (1959) assumed that at cloud base “wet” particles formed on nuclei smaller than 0.12  $\mu\text{m}$  were at equilibrium at 100% relative humidity (RH), and the particles formed on nuclei larger than 1.2  $\mu\text{m}$  were at equilibrium at 99% RH. Flossmann et al. (1985) assumed that all the aerosol particles reached equilibrium with their environment at 99% RH. On the other hand, Kogan (1991) assumed that the initial droplet size formed on CCN with radii smaller than 0.12  $\mu\text{m}$  were equal to the equilibrium radius at 100% RH, while for larger ones the initial radii were specified as less than the equilibrium radii at 100% RH. To determine the size of the initial drop in the latter case, a factor  $k$  was introduced to indicate by how much the size of the dry CCN is extended.

In this study a nucleation scheme similar to Kogan (1991) was used, except that a wider size range of CCN was considered. The aerosol particles were divided into 64 categories with a minimum radius of 0.0041  $\mu\text{m}$ . Based on the previous studies (e.g., Mordy, 1959; Kogan, 1991), we assumed the condensation growth of the CCN particles with radii smaller than 0.12  $\mu\text{m}$  to be according to the Köhler equation. After reaching the critical sizes, these particles were then transferred to the cloud droplet bins where their subsequent growth was calculated based on the condensation equation. For the particles with radii larger than 0.12  $\mu\text{m}$ , a factor  $k$  was used to calculate the initial sizes of the droplets at zero supersaturation. The values of  $k$  and the initial radii employed in the present study are shown in Fig. 1. Factor  $k$  changes from 8.9 for the smaller CCN particles to 5 for the largest end of the CCN spectrum, to account for the smaller relative growth rate of the larger nuclei. The values of the factor  $k$  used by Kogan (1991) are also shown on the same plot.

2.2.2. Other microphysical processes

The immersion freezing of drops was formulated based on the measurements by Bigg (1953). According to Bigg, the number of frozen drops per unit time depends on the number of drops, their mass, and the supercooling. The parameterization given by Orville and Kopp (1977) was used in this study and the frozen drops were converted to graupel particles, if their radii were larger than 100  $\mu\text{m}$ ; otherwise, they formed ice crystals.

Nucleation of ice crystals by deposition, and condensation freezing was based on Meyers et al. (1992). At each time step, the concentration of IN that could be activated was calculated according to Meyers et al. formula, and was compared with the previous number of activated ice particles. If the latter was greater than the former, no new nucleation occurred; otherwise the difference between these two values was taken as the actual number of new ice crystals that would be formed. This procedure is similar to that applied by Clark (1974) for nucleation of drops.

Parameterization of the number of ice crystals produced by contact nucleation due to thermophoresis, diffusiophoresis, and Brownian motion was formulated according to

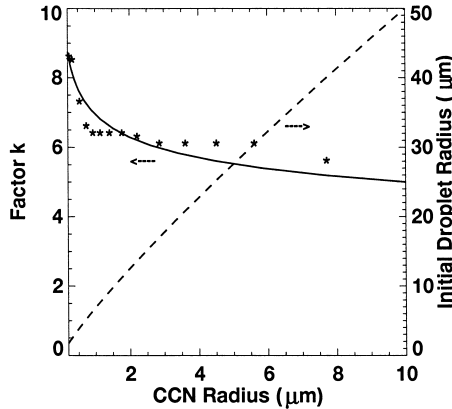


Fig. 1. Initial droplet radius and the factor  $k$  used in the calculation of the CCN nucleation process as a function of CCN radii. The  $k$  values used by Kogan (1991) are also shown as stars.

Cotton et al. (1986). Here, ice particles formed by contact nucleation had the same mass as the drops that formed them.

The ice crystals formed by either freezing of drops smaller than 100  $\mu\text{m}$  in radius, or by deposition, and condensation-freezing, were assumed to be oblate spheroids and their initial size assumed to be 5  $\mu\text{m}$  in diameter. In the present paper, the shape of the ice crystals remained unchanged with temperature, but their growth rate was allowed to vary with temperature as if the ice particles changed their shape [for details see Reisin et al. (1996b)].

The changes in the mass and number distribution functions of the drops and the ice particles due to diffusive growth/evaporation of water vapor, were calculated for each size category by analytically solving (for one time step) the kinetic diffusion equation (Tzivion et al., 1989; Reisin et al., 1992,1996b).

The model considered collision coagulation between the different species, as well as collision breakup of drops [Low and List (1982a,b) kernels]. Such interactions could lead to the transformation from one particle type to another. In this study we made the following assumptions:

1. Snow particles were formed and grew by aggregation of ice crystals.
2. Ice crystals grew by riming with drops smaller than themselves, as long as the overall rimed mass was less than the mass of the ice crystal itself; otherwise the ice crystal was transformed into a graupel particle.
3. The interactions between graupel and other particles always produced graupel.
4. Graupel particles were also created when drops collided with snow particles and with ice crystals smaller than themselves.

The collision and coalescence efficiencies used for interactions between drop–drop, drop–ice, and ice–ice were similar to those in Reisin et al. (1996b). For collision between drops, the kernel of Low and List (1982a,b) are used for raindrops larger than 0.6 mm; the coalescence efficiencies of Ochs et al. (1986) are employed as collection efficiencies (assuming that the collision efficiencies in this region are close to unity) in the region 0.1–0.6 mm; the collision efficiencies of Long (1974) are adapted for smaller drops. The collision efficiencies between graupel particles and drops are calculated according to Hall (1980) and Rasmussen and Heymsfield (1985). For ice crystals (plates) colliding with drops we used collision efficiencies given by Martin et al. (1982) and for large supercooled drops colliding with planar ice crystals we used the coefficients calculated by Lew et al. (1985). The data sets for ice and drop as collectors were combined to give a full set of size ranges. But, there is not enough information to cover the whole size range required by the model. An approach suggested by Chen (1992) was used to fill the gaps in the data. This approach was based on the fact that the collision efficiency reaches a minimum when the drop being collected reaches a size such that its fall velocity approaches that of the collector ice particle, and that for drops of even larger sizes, the relative velocity between drop and ice crystal changes sign and the collision efficiency increases again. A mirror image about the minimum of the collision efficiencies was assumed so that interpolations could be made between existing data. For a collector-drop size larger than that given by Lew et al. (1985), the collision

efficiencies remain virtually unchanged and have been assumed to be constant for a fixed ice crystal size. Coalescence efficiencies for interaction between ice particles are used in accordance with Wang and Chang (1993), in which the dependence on temperature was considered.

The Hallett–Mossop mechanism for secondary ice production was parameterized according to Mossop (1978), in which the number of ice crystals produced per second was formulated as a function of the number of large drops ( $\geq 24.8 \mu\text{m}$ ) and small drops ( $\leq 12.3 \mu\text{m}$ ) collected per second by a graupel particle. The temperature dependence of this process was taken from Cotton et al. (1986), where the maximum occurs at  $\sim -5^\circ\text{C}$ .

The kinetic equation for the melting of graupel particles was treated in the same way as the evaporation, except that the rate of change of mass of a melting graupel depended on temperature (Rasmussen and Heymsfield, 1987). We assumed complete shedding of the melted mass for the graupel particles. Snowflakes and ice crystals were assumed to melt instantaneously whenever they entered a region in which the environmental temperature was above  $0^\circ\text{C}$ .

Sedimentation of both drops and ice particles was calculated using Smolarkiewicz (1983) positive advection scheme. The parameters for terminal fall velocity of drops were according to Beard (1977) and for the ice particles based on Böhm (1989).

The grid dimensions of the model were set to 300 m both in the horizontal and the vertical directions (separate experiments indicated that the simulation results were not sensitive to the changes in the grid size). The vertical and the horizontal dimensions of the domain were 12 and 30 km, respectively. The time step was 5 s for dynamic and the microphysical processes except for the diffusive growth/evaporation (or sublimation) processes of hydrometeors, in which a time step of 2.5 s was used.

### 3. Description of the experiments and initial conditions

The initial total aerosol spectrum was based on the measurements carried out in Montana, USA, by Hobbs et al. (1985). We fitted this spectrum by superimposing three lognormal distributions as:

$$\frac{dN}{d\ln r_n} = \sum_{i=1}^3 \frac{n_i}{(2\pi)^{1/2} \log \sigma_i \ln 10} \exp\left(-\frac{[\log(r_n/R_i)]^2}{2(\log \sigma_i)^2}\right). \tag{9}$$

The parameters of the distributions were similar to those used by Respondek et al.

Table 1

Parameters for the aerosol particle distribution:  $n_i$  = total number of aerosol particles per cubic centimeter of air,  $R_i$  = geometric mean aerosol particle radius in  $\mu\text{m}$ ,  $\sigma_i$  = standard deviation in mode  $i$

Mode $i$	$n_i$	$R_i$	$\log \sigma_i$
1	40 000	0.006	0.3
2	3980	0.03	0.3
3	0.3	0.3	0.396

Table 2

Percentages of water soluble particles in modes 1, 2 and 3, and the CCN concentrations in the three classes (N1:  $r_N < 0.1 \mu\text{m}$ ; N2:  $0.1\text{--}1.0 \mu\text{m}$ ; N3:  $r_N > 1.0 \mu\text{m}$ ; see text for explanations). The concentration is in  $\text{cm}^{-3}$

Experiment	Mode 1	Mode 2	Mode 3	N1	N2	N3
MR0	0.2	8	0.0	171.5	5.30	0.0
MR1	0.2	8	50	171.5	5.34	0.02
CN0	5	20	0.0	1029.8	13.25	0.0
CN1	5	20	50	1029.8	13.30	0.02
EC0	10	20	0.0	1697.6	13.27	0.0
EC1	10	20	50	1697.6	13.31	0.02
EC2	10	20	100	1697.6	13.36	0.05

(1995) and are given in Table 1. The concentration was assumed to decrease with height according to:

$$N(z, r_n) = N(z = 0, r_n) \times \exp(-z/z_s), \quad (10)$$

where,  $z_s$  was the scale height and set to 2 km in this study.

As mentioned above, because the main objective here was to study the effects of size distributions of CCN on the development of mixed convective clouds, the variations of the chemical compositions of the aerosol particles were not considered. Instead, the CCN spectra were created by simply assuming different percentages of total aerosol particles to be water-soluble. In addition, all the CCN particles were assumed to be composed of ammonium sulfate. This assumption was also based on the previous studies (e.g., Fitzgerald, 1974; Takeda and Kuba, 1982) which showed that the differences in the chemical composition of CCN (such as NaCl, and  $(\text{NH}_4)_2\text{SO}_4$ ) do not significantly change the predicted size distribution of cloud droplets. The fractions of water soluble particles ( $\varepsilon$  in Eq. 8 multiplied by 100) and the CCN number for each class are shown in Table 2 and all the initial CCN distributions are given in Fig. 2. The experiments were divided into three groups, ‘maritime’(MR), ‘continental’(CN), or ‘extreme-continental’(EC), based on their CCN concentrations. In each group at least two cases were studied. In the first set of experiments, MR0, CN0 or EC0 (hereafter, control cases), the initial CCN were assumed to contain particles only from the first two modes of aerosol

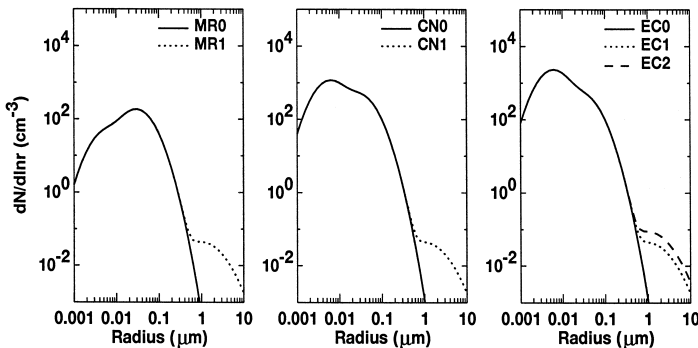


Fig. 2. Initial CCN distributions employed in the present study. See text for explanation.

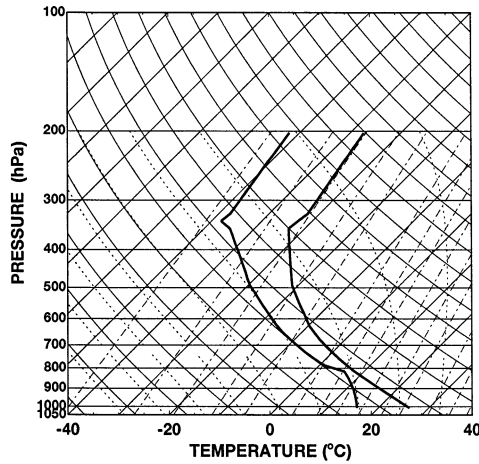


Fig. 3. Vertical profiles of temperature and dew point used in the present work.

distributions, while the third mode was assumed to be water insoluble. In the second set, MR1, CN1 or EC1, the concentration of the Aitken and large particles were left as before but a third mode was added, which contained 50% soluble particles ( $\sim 23 \text{ l}^{-1}$ ). In the extreme-continental group, a third case (EC2) with twice the concentration of giant CCN was also tested.

The initial thermodynamic conditions for all reported tests here were given by a theoretical profile of temperature and dew point as shown in Fig. 3. The temperature, dew point temperature, and pressure at the surface were  $26^\circ\text{C}$ ,  $15.8^\circ\text{C}$ , and  $1007 \text{ hPa}$ , respectively. For initialization, a pulse of heat that produced a  $2^\circ\text{C}$  perturbation was applied for one time step at  $t = 0$  at a height of  $600 \text{ m}$ , and at the center of the domain. The possible influence of wind shear was not considered in the present study.

## 4. Results

Numerical simulations were carried out until the cloud dissipated (usually  $60 \text{ min}$  from model initiation). In all the cases the cloud base and top were at  $1.5 \text{ km}$  ( $11^\circ\text{C}$ ) and  $7.2 \text{ km}$  ( $-28^\circ\text{C}$ ), respectively. The  $0^\circ\text{C}$  isotherm was at  $2.7 \text{ km}$ . The base and the top of the cloud were defined as the place where the total mixing ratio of the hydrometeors was greater than  $0.01 \text{ g kg}^{-1}$  (as Orville and Kopp, 1977). The rain initiation was defined as the time at which the maximum rainfall rate at the surface began to exceed  $0.1 \text{ mm h}^{-1}$ .

A summary of the main results obtained for seven runs is presented in Table 3. Below, we compare the cases for each group.

### 4.1. Continental clouds (CN)

Two cases (CN0 and CN1) were calculated for continental clouds. The general appearance of these two clouds in the developing stage was similar. The clouds began to form  $15 \text{ min}$  after the model initialization, and continued to develop very rapidly after their top reached the  $-5^\circ\text{C}$ . This is attributed to a larger extent to the environmental

Table 3

The main results obtained from seven runs (time is given in minutes from the initiation of the calculations and the height is in km)

Feature	MR0	MR1	CN0	CN1	EC0	EC1	EC2
Max. updraft ( $\text{m s}^{-1}$ )	17.2	17.1	16.5	16.5	16.3	16.3	16.2
Time and height	33, 4.2	33, 4.2	33, 3.9	33, 4.2	33, 3.9	33, 3.9	33, 3.9
Max. LWC ( $\text{g kg}^{-1}$ )	5.13	4.75	5.28	4.58	5.28	4.58	4.59
Time and height	33, 4.8	33, 4.8	34, 5.4	33, 4.8	34, 5.4	33, 4.8	33, 4.5
Max. number of drops ( $\text{cm}^{-3}$ )	176.0	175.8	743.4	729.2	1134	1102	1080
Time and height	27, 2.1	27, 2.1	30, 3.6	29, 3.3	30, 3.6	30, 3.6	30, 3.3
Max. ice mass ( $\text{g kg}^{-1}$ )	0.88	0.90	0.25	0.38	0.44	0.48	0.42
Time and height	60, 5.7	60, 5.7	54, 6.0	53, 6.0	54, 6.0	53, 6.0	52, 6.0
Max. graupel mass ( $\text{g kg}^{-1}$ )	5.72	5.80	3.21	3.77	2.58	3.63	3.99
Time and height	46, 3.0	44, 3.0	40, 5.4	40, 3.9	41, 5.1	40, 3.9	39, 4.5
Max. ice number ( $\text{l}^{-1}$ )	73.40	74.60	21.23	23.97	20.63	22.90	23.50
Time and height	46, 5.7	46, 5.7	37, 6.9	37, 6.9	37, 6.9	37, 6.9	37, 6.9
Max. graupel number ( $\text{l}^{-1}$ )	8.58	7.35	6.19	1.60	3.98	0.63	0.68
Time and height	37, 6.6	37, 6.6	38, 6.6	39, 6.6	40, 6.3	39, 6.6	37, 6.3
Max. mass of drops [ $D > 1 \text{ mm}$ ] ( $\text{g kg}^{-1}$ )	3.23	3.50	1.27	2.12	0.45	1.86	2.12
Time and height	48, 0.0	47, 0.0	51, 0.0	46, 0.0	49, 0.0	45, 0.0	44, 0.0
Max. number of drops [ $D > 1 \text{ mm}$ ] ( $\text{l}^{-1}$ )	1.99	2.05	1.20	1.56	0.54	1.46	1.63
Time and height	49, 0.0	47, 0.0	51, 0.0	46, 0.0	49, 0.0	46, 0.0	45, 0.0
Max. graupel mass [ $D > 1 \text{ mm}$ ] ( $\text{g kg}^{-1}$ )	5.72	5.80	3.15	3.77	2.53	3.63	3.99
Time and height	46, 3.0	44, 3.0	40, 5.4	40, 3.9	41, 5.1	40, 3.9	39, 4.5
Max. graupel number [ $D > 1 \text{ mm}$ ] ( $\text{l}^{-1}$ )	1.05	0.92	1.10	0.32	0.82	0.28	0.35
Time and height	36, 6.0	36, 5.7	39, 6.0	37, 6.0	41, 5.7	37, 6.0	37, 6.0
Time of rain initiation	38	36	41	36	42	36	35
Max. radar reflectivity (dBZ)	67.6	68.0	59.9	64.4	55.5	63.4	64.0
Time and height	46, 3.6	46, 3.3	45, 3.3	41, 3.0	42, 4.2	39, 4.5	39, 4.2
Max. rain rate ( $\text{mm h}^{-1}$ )	187.0	196.9	59.0	101.5	21.3	86.1	100.1
Time	49	48	51	46	50	45	45
Max. accumulated rain (mm)	27.25	29.18	7.76	12.45	2.57	10.27	12.05

thermodynamic conditions and to a lesser extent to the more latent heat released by formation of ice phase hydrometeors (ice nucleation by deposition and condensation-freezing started at temperatures lower than  $-5^\circ\text{C}$ ). The clouds reached their maximum development 33 min from model initialization (Table 3) and the maximum updraft was  $16.5 \text{ m s}^{-1}$ .

Although the dynamic structure was similar, many of the microphysical properties were different (Table 3). Fig. 4 shows the mass and number distribution functions of the drops at the cloud center, at 1800 m height (just above cloud base), and after 16 min of simulation (corresponding to the stage of cloud initiation) in CN0 (heavy line) and CN1 (thin line). It is obvious from this figure that although their numbers were relatively small, the droplets nucleated on giant CCN in case CN1, had a considerable effect on developing a wider mass distribution, and forming large drizzle drops. In comparison,

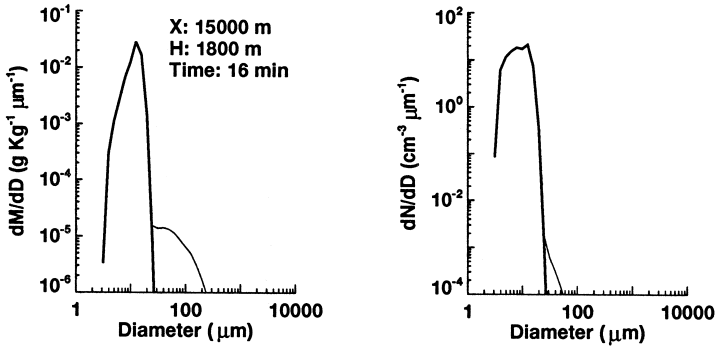


Fig. 4. Mass (left) and number (right) distribution functions of drops for case CN0 (heavy line) and CN1 (thin line) at the center of the clouds, 1800 m high (just above the cloud base), and at 16 min of simulation.

the spectra in CN0 were much narrower. The subsequent evolution of the drop size distributions at different locations in the clouds after 32 and 36 min (corresponding to the stages of maximum development and rain initiation, respectively) are shown in Fig. 5. At 32 min, much more pronounced second (even third in some of the points) modes developed in most parts of the cloud (~ 3–4 km) in case CN1, while in CN0 the second mode began to form only in the upper parts of the cloud (above 4 km). These results

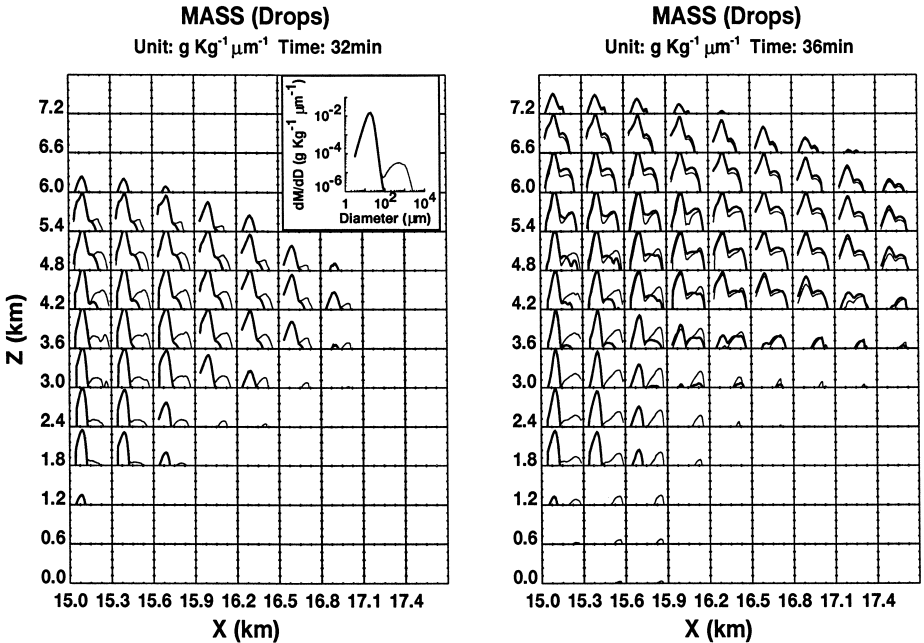


Fig. 5. Mass distribution functions of drops in case CN0 (heavy line) and CN1 (thin line) at different spatial points, and after 32 min (left) and 36 min (right) of simulations. In order to better see the coordinates, one of the panels is enlarged. Because the clouds were symmetric about their centers, only the right halves are shown here.

demonstrate that the coalescence process in CN1 began to operate earlier and more efficiently than that in CN0. Because larger drops developed earlier in CN1, they descended to the lower reaches of the cloud after 36 min. In contrast, in CN0 at the same time, most of the large drops were still growing in the middle and upper parts of the cloud.

Consistent with the development of the drop size distributions, the cloud in CN1 reached its maximum LWC, 1 min earlier and 600 m lower than that in CN0, but the values of maximum LWC and drop number were smaller in CN1 than in CN0. These results show that the inclusion of giant CCN in CN1 inhibited the nucleation of some of the smaller CCN and accelerated the growth of precipitation by transferring more liquid water to millimeter size raindrops (Table 3).

Comparison of the graupel production between case CN0 and CN1 is given in Fig. 6. In CN1, graupel particles initially formed at 32 min of simulation near the 5 km ( $\sim -15^{\circ}\text{C}$ ) level reached their maximum mass of  $3.77 \text{ g kg}^{-1}$  at the height of 3.9 km after 40 min. Whereas in CN0, graupel began to appear after 35 min and at the height around 6 km, 3 min later and 1 km higher than that in the former case. Although the maximum graupel mass was reached at the same time in these two cases, the value was lower and occurred at a higher level in CN0 than that in CN1. Different from the evolution of graupel mass, the graupel concentration reached a peak of only  $1.6 \text{ l}^{-1}$  in CN1, much lower than that in CN0 ( $6.19 \text{ l}^{-1}$ ). The comparatively larger mass and lower

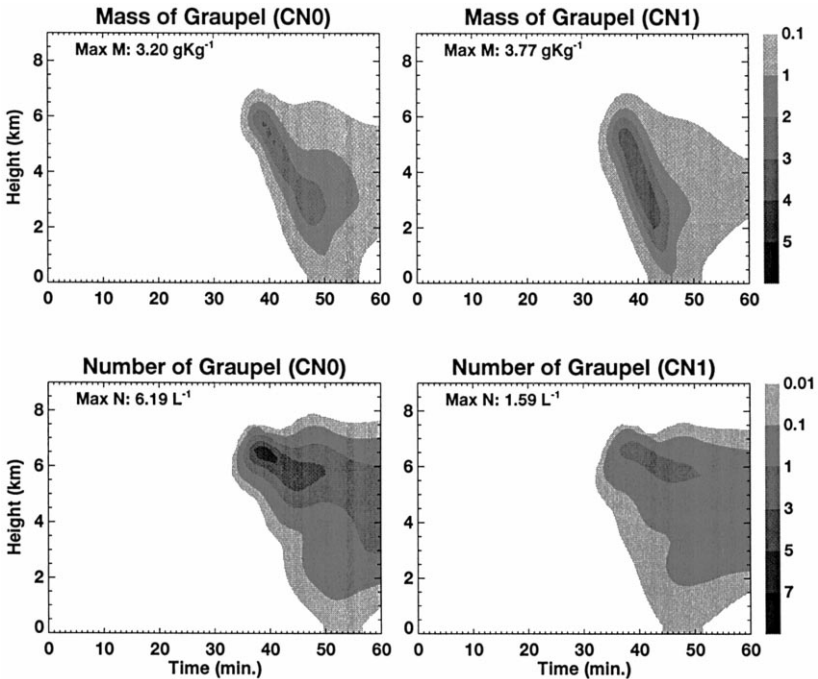


Fig. 6. Time–height cross sections of mass (upper) and concentration (lower) of graupel particles for case CN0 (left) and CN1 (right). The unit used and maximum value obtained are shown at the upper left corner of each panel.

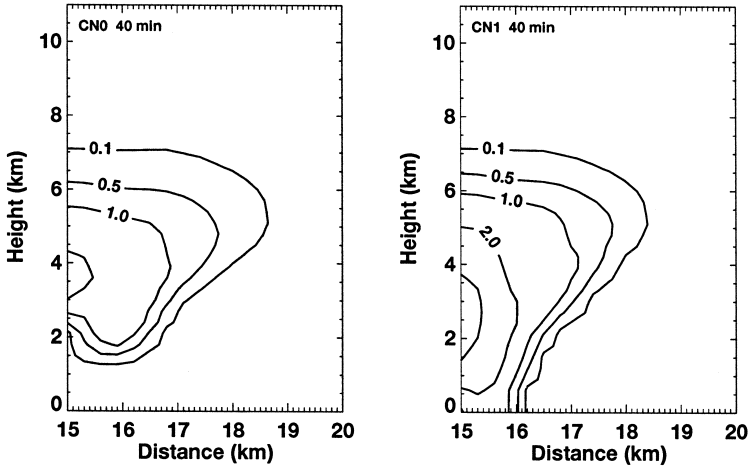


Fig. 7. Spatial distribution of the effective radii of graupel particles at 40 min in case CN0 (left) and CN1 (right). Unit: mm.

concentration of graupel in CN1 correspond to larger sizes than those in CN0, as can be seen in Fig. 7.

Fig. 7 shows the spatial distribution of the effective radii of graupel particles at 40 min (corresponding to the maximum development of graupel content). It can be seen that larger graupel particles ( $r_{\text{eff}} > 2$  mm) appeared in the lower part of the cloud in case CN1, while they were almost absent in CN0. In addition, the figure shows that some of the large graupel particles had already fallen to the ground in CN1. In CN0, on the other hand, all the particles were still being lifted in the middle and upper parts of the cloud. Because of their relatively small sizes, the particles ( $r_{\text{eff}} < 0.5$  mm) in CN0 were also carried farther away from the main updraft core.

The difference in the content and concentration of ice crystals between CN0 and CN1 can be found in Table 3. Compared with CN0, more ice crystals were produced in CN1.

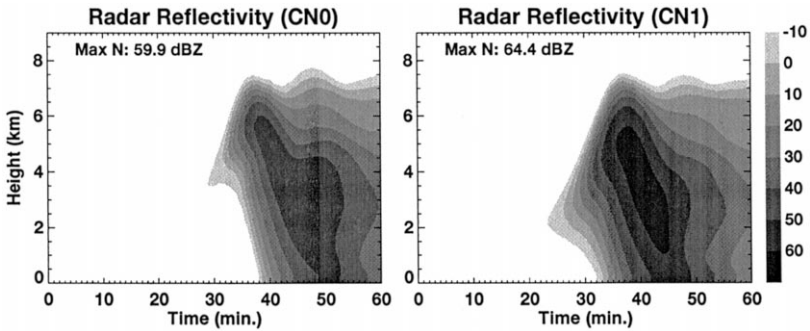


Fig. 8. Time–height cross sections of the radar reflectivity at cloud center for cases CN0 (left) and CN1 (right).

This is due to the higher supersaturation with respect to ice in CN1, which enhanced the formation of ice crystals by deposition and condensation-freezing, and the relatively large graupel particles and drops, which made the secondary ice production process more active. However, the differences in the concentration and mass of ice crystals were not significant as that of drops and graupel particles.

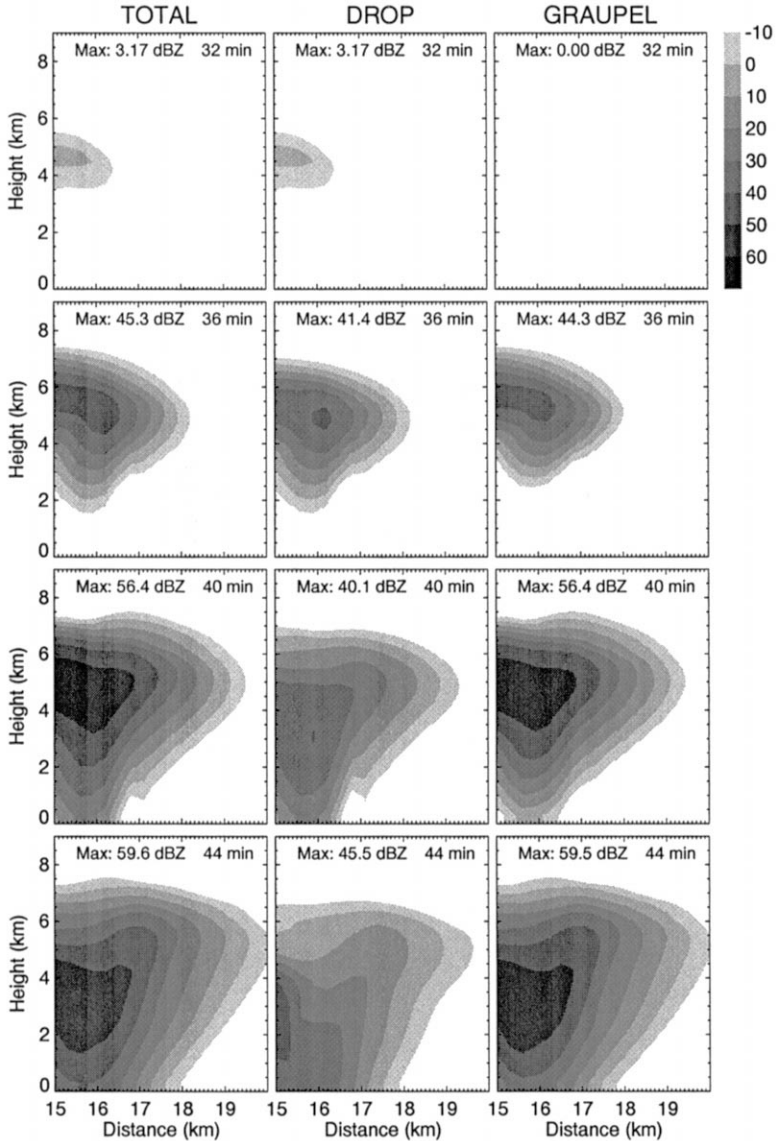


Fig. 9. The total radar reflectivity (left), the contribution of water drops (middle), and the contribution of graupel particles (right) at 32, 36, 40, and 44 min from model initiation in case CN0 (because the cloud was symmetric about the center of the domain, only half of the graphs are shown here).

The time–height cross sections of the radar reflectivity in cases CN0 and CN1 are presented in Fig. 8. The  $-10$  dBZ echo developed about 5 min earlier in CN1 than that in CN0, and the maximum echo reached about 5 dBZ higher in the former. It is also noted that in CN1 the initial radar reflectivity appeared at a lower height. The relative contributions of water drops and graupel particles to the total radar reflectivity are shown in Fig. 9 for CN0 and Fig. 10 for CN1.

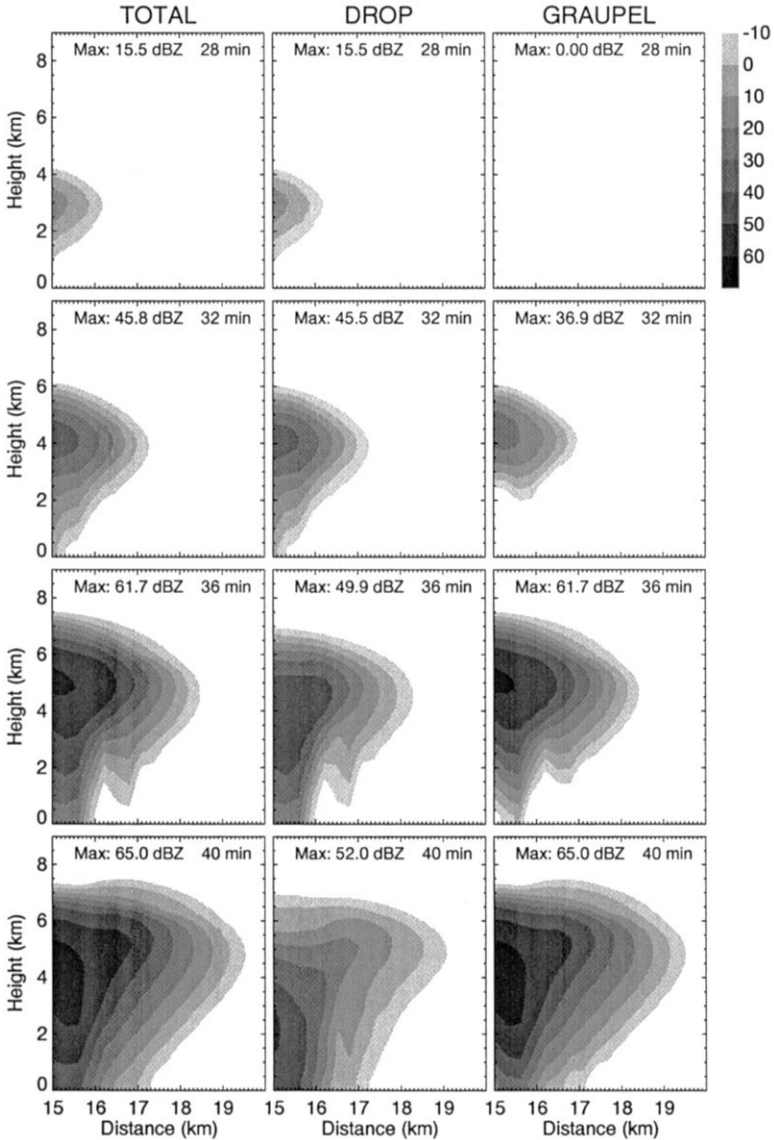


Fig. 10. The total radar reflectivity (left), the contribution of water drops (middle), and the contribution of graupel particles (right) at 28, 32, 36, and 40 min from model initiation in case CN1.

In case CN0, the first echo appeared at 32 min from model initiation (16 min after cloud formation) and was mainly produced by graupel particles. Only at the very beginning stage, the contribution from supercooled water was more than that from graupel. In case CN1, however, the initial echo appeared at 26 min of simulation due to the early growth of the large drops. Although the echo from the graupel particles became very strong about 10 min later, the total contribution to the radar reflectivity was nearly equally shared by both types of hydrometeors.

Consistent with the development of precipitation particles, rain in case CN1 started 5 min earlier, reached a higher intensity, and produced more rain on the ground than that in CN0.

#### 4.2. Maritime clouds (MR)

Two simulations (MR0 and MR1) were performed for the maritime clouds. Here, one must keep in mind that the term ‘maritime cloud’ in this study only refers to the relatively small initial CCN concentration.

The clouds simulated in these two cases had the same dynamic structure, in terms of maximum updrafts and the time and altitude of these maximums (Table 3). Both clouds reached their peak liquid water content after 33 min of simulation at a height of 4.8 km. The maximum mass in case MR0 and MR1 was 5.13 and 4.75 g kg<sup>-1</sup>, respectively. Although the inclusion of giant CCN slightly reduced the liquid water content, the maximum drop concentration was almost the same in these two cases. This fact can be explained by the evolution of the drop size distribution. Figs. 11 and 12 show the drop size distribution of case MR0 and MR1 at 16 and 36 min, respectively. Comparing these figures with the corresponding ones in continental clouds (Figs. 4 and 5) reveals that when the CCN concentration in the Aitken and large size mode were low (maritime clouds) — although inclusion of giant CCN produces a few large drops at the initial stage (16 min) of the cloud — the droplets formed on large CCN caught up with them due to their rapid growth under the higher supersaturation (compared to the continental clouds) produced in the updraft region. In addition, because the drops formed on the

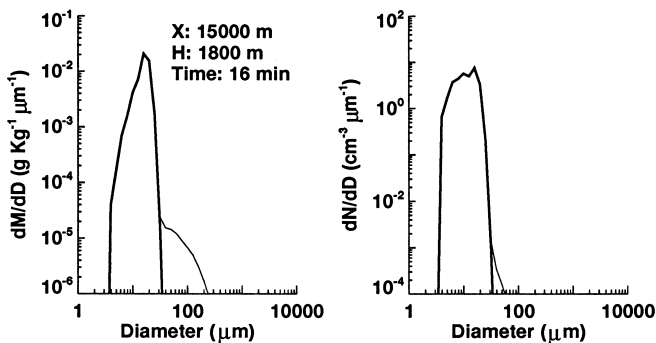


Fig. 11. Mass (left) and number (right) distribution functions of drops for case MR0 (heavy line) and MR1 (thin line) at the clouds center, 1800 m high (just above the cloud base), and at 16 min of simulation.

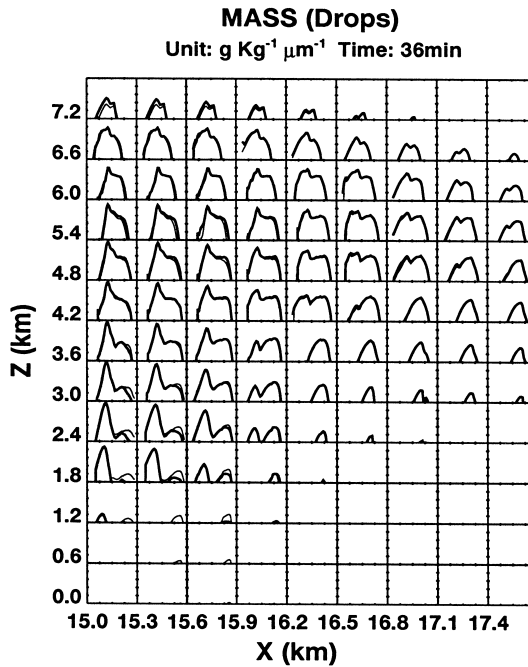


Fig. 12. Mass distribution functions of drops in case MR0 (heavy line) and MR1 (thin line) at different spatial points, and at 36 min of simulations.

large CCN were more numerous than those formed on giant CCN, they dominated the subsequent collection of drops, and reduced the relative advantage of the latter. This fact can also be seen from the similar development of the graupel particles in Table 3.

In both cases, the graupel particles began to form at 31 min, and 6 min later the peak concentration appeared at 6.6 km. The maximum graupel number in case MR0 and MR1 were 8.58 and 7.35  $\text{l}^{-1}$ , and maximum masses were 5.72 and 5.80  $\text{g kg}^{-1}$ , respectively. The peak values were located at the same altitude (Table 3). Due to the similarity of the development of the precipitation particles, the evolution of the radar reflectivity (not shown) was also very similar (maximum radar reflectivity in case MR0 and MR1 were 67.6 and 68 dBZ, respectively). A small difference in the height of the maritime echo appeared in MR1 that occurred about 0.3 km lower. Table 3 shows that the time of rain initiation, rainfall rate and accumulated rain were similar in MR0 and MR1. In summary, the effects of introducing giant CCN to maritime clouds were relatively small.

#### 4.3. Extreme-continental clouds (EC)

Three simulations (EC0, EC1 and EC2) were conducted for the extreme-continental clouds in order to investigate (i) how the giant CCN influence the development of precipitation particles when the concentration of smaller CCN is high; and (ii) what are the consequences when the concentration of giant CCN is increased.

Although different number of giant CCN were included in the initial CCN spectra, the developments of the cloud dynamic structures in these three cases were almost the same and also very similar to the continental cases described before. The clouds reached their maximum development at 33 min of simulation and the peak updraft was  $16.3 \text{ m s}^{-1}$ , located at 3.9 km high. As expected, more significant differences, compared with the continental cases, appeared in the development of the hydrometers between the control case and the case with giant CCN.

#### 4.3.1. Comparison between case EC0 and EC1

The time–height cross sections of drops and graupel particles at the clouds center are shown in Figs. 13 and 14. Although in both cases, cloud began to form at the same time the cloud reached its maximum LWC earlier and located at a lower altitude in EC1 than in EC0, and maximum value was smaller in the former case than in the latter. The maximum drop number in case EC1 was also slightly lower than that in EC0.

The most striking differences are exhibited in the development of graupel particles. The inclusion of giant CCN in EC1 accelerated the growth of drops by collision-coalescence mechanism. At the same time, this also reduced the overall concentration of the drops. Therefore, when the drops were lifted above zero degree level, the concentration

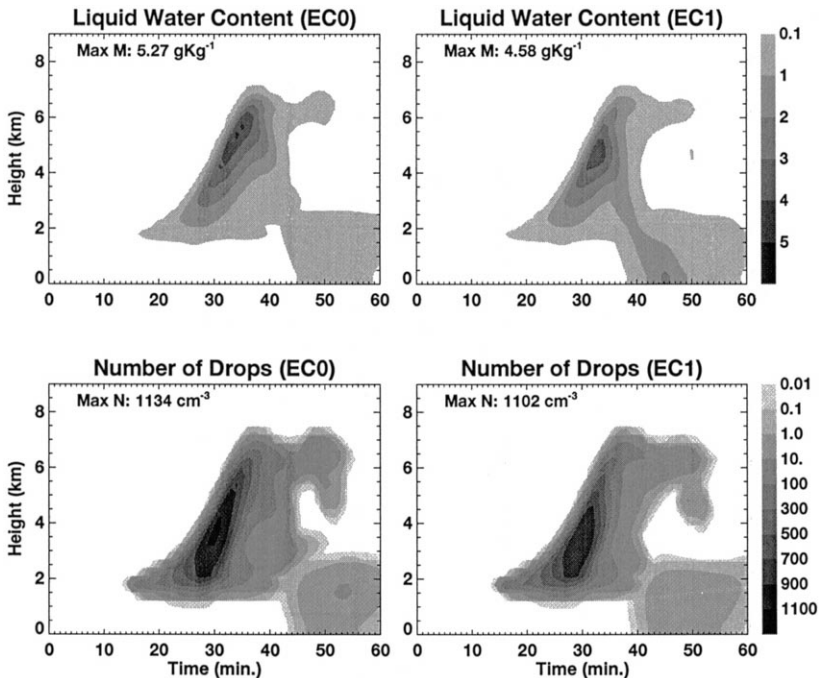


Fig. 13. Time–height cross sections of liquid water content (upper) and drop number (lower) at cloud center for case EC0 (left) and EC1 (right). The unit used and maximum value obtained are shown at the upper left corner of each panel.

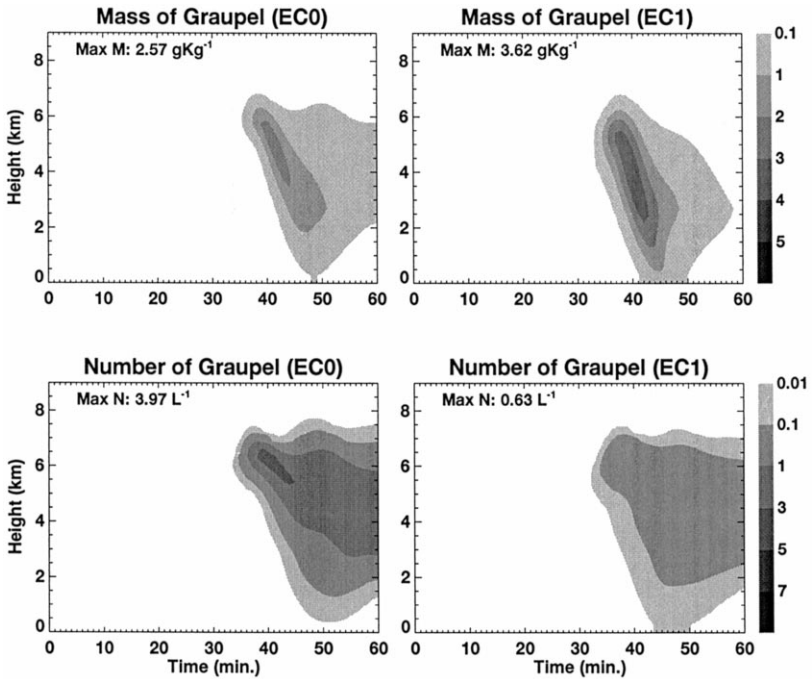


Fig. 14. Time–height cross sections of graupel content (upper) and number (lower) at cloud center for case EC0 (left) and EC1 (right). The unit used and maximum value obtained are shown at the upper left corner of each panel.

of graupel particles formed by self-freezing and interactions between drops and ice particles was lower in EC1 than in EC0. This is manifested in the results shown in Table 3, that is, the concentration of graupel particles in EC1 only reached a maximum of 0.63 l<sup>-1</sup>, much lower than that in EC0, 4 l<sup>-1</sup>. On the other hand, the graupel mass in EC1 reached a maximum of 3.63 g kg<sup>-1</sup>, higher than in EC0, 2.58 g kg<sup>-1</sup>. The location of peak value was also 1.2 km lower in EC1 than in EC0.

Comparison of the radar reflectivity between case EC0 and EC1 is presented in Fig. 15. Consistent with the development of precipitation particles the radar reflectivity in case EC1 grew faster and reached a higher peak echo than in case EC0. The difference of radar reflectivity between EC1 and EC0 was 8 dBZ, again larger than in the continental cases, 4.5 dBZ, and in maritime cases, 0.4 dBZ.

These results indicate that the differences in precipitation particles produced by inclusion of giant CCN in extreme-continental clouds are more significant than that in the moderate continental clouds. This is also expressed in the earlier initiation of rain (almost 6 min) in EC1 (see Table 3), and the higher rain intensity. The maximum rain intensity increased by a factor of three due to the inclusion of giant CCN (case EC1), the corresponding values in the continental case CN1 was 72%, and in maritime case (MR1) only 5%. The maximum accumulated rain at the surface in case EC1 was 10.27 mm, four times higher than in case EC0.

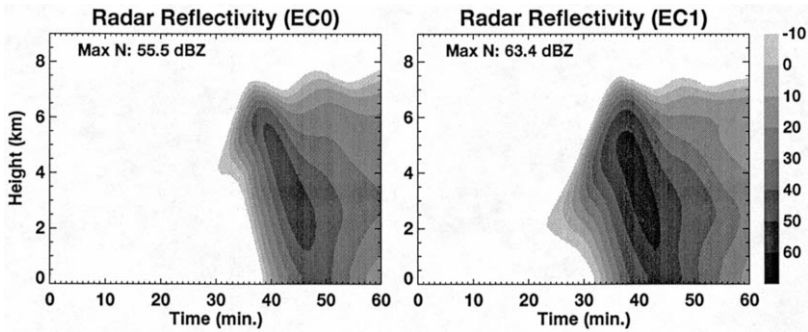


Fig. 15. Time–height cross sections of the radar reflectivity at cloud center for cases EC0 (left) and EC1 (right).

#### 4.3.2. Comparison between case EC2 and EC1

In EC2 the concentration of giant CCN in the reference case EC0 was doubled. The main results obtained from this simulation are listed in Table 3. It can be seen that the dynamic fields such as updraft and LWC in case EC2 were very similar to EC1, but the differences between EC2 and EC0 were more pronounced than that between EC1 and EC0. Both the content and concentrations of raindrops and graupel particles were increased with increasing concentration of giant CCN. The results in Table 3 also show that with increased concentration of giant CCN, the rain started earlier, reached higher intensity and produced more total rain on the ground. Correspondingly, the radar reflectivity also reached higher values. One should also note, however, that although increase in the concentration of giant CCN results in more precipitation at the surface, too many giant CCN could lead to stronger competition among the droplets formed on them, leading to reduction of precipitation.

## 5. Discussion and conclusions

The principal conclusions of this study are that inclusion of giant CCN produces a tail of large drops in the cloud droplet distribution near cloud base. The effects of these large drops are significant when the concentration of small nuclei is high, as that in continental or especially, in extreme-continental clouds. Under these conditions, the inclusion of giant CCN accelerates coalescence between water drops, leading to an early development of large drops at the lower parts of the clouds. It also leads to the formation of larger graupel particles and more intensive radar reflectivity. When the concentration of small nuclei is low, as that in maritime clouds, the effect of the giant CCN is small and the development of precipitation is dominated by the droplets formed on large nuclei. We will elaborate these points further below.

Inclusion of giant CCN always produces a few large droplets at the cloud initiation stage. This is seen in the size distribution plots (e.g., Figs. 4 and 11). But how these large droplets influence the subsequent development of raindrops and other hydrometeors is to a large extent dependent on the initial concentration of smaller CCN, especially the concentration of Aitken nuclei. In continental clouds in which the concentration of

CCN is high, the droplets grow slow because of their higher concentrations and the increased competition for the available supersaturation produced by the updrafts. As a result, raindrops cannot be formed effectively by the collision and coalescence process and the cloud exists in a colloidal stable state. In this case, the large droplets formed on giant CCN serve as an inherent destabilizing factor, which accelerates the collision and coalescence between drops in the lower parts of the clouds. This is seen in the drop size distributions and radar reflectivity in Section 4.1. In contrast, in maritime clouds in which the concentration of smaller CCN is low, the droplets formed on large CCN grow rapidly due to the low concentration of total droplets and the reduced competition for the available water vapor. Because they are more numerous than the drops formed on giant CCN, these drops dominate the subsequent collection process. This means that the relative advantage or “Head start” of the drops formed on the giant CCN is reduced.

The role of the giant CCN is not only in the development of larger drops but also in the acceleration of precipitation development through the ice phase. As was shown here, precipitation is produced in the extreme-continental cloud even without the presence of giant CCN. This is due to the formation of ice by nucleation. But the important conclusion here is that the initiation time, the location, and the quantity of these precipitation particles is very much different when even a few giant CCN are presented. This can be attributed to the fact that both the freezing and accretion processes are dependent on the drop sizes under the same thermodynamic conditions. The relatively large drops formed in the case with giant CCN produce graupel particles earlier. Because of their higher coagulation efficiency with drops, these early appearing graupel particles capture more droplets and grow faster as they are lifted in the updraft region. In addition, because of their larger size, these graupel particles are not lifted to higher altitudes and remain closer to cloud base. In contrast, in the control case, the more numerous but smaller drops are transported to the upper parts of the cloud where they grow or form ice particles by freezing or through interaction with ice particles. Since these particles are smaller in size, they are also carried farther away from the updraft core by the divergent flow that exists in the upper reaches of the cloud.

When large drops are carried into the supercooled regions, ice multiplication processes may also take effect under suitable temperature conditions. As has been indicated in the previous section, inclusion of giant CCN leads to the formation of large drops and graupel particles that develop earlier and at lower levels in the clouds, and this in turn increases the opportunities for ice multiplication. This may explain the reason why more ice crystals are produced in the cases when giant CCN are included.

The results presented in this paper are based on a specific thermodynamic profile, which represents a moderate convective cloud with relatively warm cloud base (11°C). Although the principal effects of the giant CCN on cloud and precipitation development are not expected to be much different under different atmospheric conditions, more numerical experiments are needed to draw a firm conclusion.

## Acknowledgements

We would like to thank Mekorot Water of Israel and its subsidiary E.M.S, for partially funding this research. Thanks are also due to Mr. and Mrs. L. Ross for their

contribution to the laboratory, which made part of this work possible. Comments by Professor K.D. Beheng helped us clarify some important points and improved the quality of this paper. We thank him for that. Part of the calculations was carried out using the Cray J932 computer of Inter University Computer Center, Israel.

### Appendix A. Dynamic equations of the model

The vertical and horizontal velocity were calculated based on the stream function and vorticity equation as follows:

$$\frac{\partial \zeta}{\partial t} + D(\zeta) = \frac{1}{\rho_0} \frac{\partial \rho_0}{\partial z} w \zeta + \frac{\partial}{\partial z} F_d(u) - \frac{\partial}{\partial x} F_d(w) - g \frac{\partial}{\partial x} \left( \frac{\theta_v}{\theta_{v_0}} - \sum_{y=w,i,g,s} M_y \right), \quad (A1)$$

where,

$$\zeta = \frac{\partial u}{\partial z} - \frac{\partial w}{\partial x} = \frac{\partial}{\partial z} \left( \frac{1}{\rho_0} \frac{\partial \psi}{\partial z} \right) + \frac{1}{\rho_0} \frac{\partial^2 \psi}{\partial x^2}, \quad (A2)$$

then  $u$  and  $w$  components of the wind speed can be calculated by

$$u = \frac{1}{\rho_0} \frac{\partial \psi}{\partial z}, w = - \frac{1}{\rho_0} \frac{\partial \psi}{\partial x} \quad (A3)$$

$\psi$  is the stream function,  $\theta_v$  the virtual potential temperature deviation from the environmental virtual potential temperature  $\theta_{v_0}$ , and  $M_y$  ( $y = w, i, g, s$ ) are the specific liquid and solid water contents ('i' for ice crystals, 'g' for graupel particles, and 's' for snow particles).

The prediction equations for the virtual potential temperature perturbation  $\theta_v$ , the specific vapor perturbation  $q$ , the concentration and mass of a specific bin for water drops and ice particles,  $N_{w_k}$  and  $M_{w_k}$  and the CCN size distribution function  $n_{CCN_k}$  were similar to those in Reisin et al. (1996b), except that the definitions of advective and turbulent diffusion operators,  $D(\phi)$  and  $F_{d,q}(\phi)$ , were different in the present model and can be expressed as:

$$F_{d,q}(\phi) = \frac{\partial}{\partial x} \left( \nu_{d,q} \frac{\partial \phi}{\partial x} \right) + \frac{1}{\rho_0} \frac{\partial}{\partial z} \left( \rho_0 \nu_{d,q} \frac{\partial \phi}{\partial z} \right), \quad (A4)$$

$$D(\phi) = \frac{\partial(u\phi)}{\partial x} + \frac{1}{\rho_0} \frac{\partial(\rho_0 w \phi)}{\partial z}, \quad (A5)$$

$\phi$  being an arbitrary function;  $\nu_{d,q}$  is the turbulent coefficient based on the approach of Monin and Yaglom (1968):

$$\nu_{d,q} = \nu_0 + (C_{t,d,q} \Delta)^2 |\nabla[(u^2 + w^2)^{0.5}]|, \quad (A6)$$

where

$$|\nabla(\phi)| = \left[ \left( \frac{\partial\phi}{\partial x} \right)^2 + \left( \frac{\partial\phi}{\partial z} \right)^2 \right]^{0.5}. \quad (\text{A7})$$

The value of  $C_t$  was chosen to make the simulations stable as was done in Reisin et al. (1996b).

## References

- Arnason, G., Greenfield, R., 1972. Micro- and macro-structure of numerically simulated convective clouds. *J. Atmos. Sci.* 29, 342–367.
- Beard, K.V., 1977. Terminal velocity adjustment for cloud and precipitation. *J. Atmos. Sci.* 34, 1293–1298.
- Bigg, E.K., 1953. The formation of atmospheric ice crystals by the freezing of droplets. *Q. J. R. Meteorol. Soc.* 79, 510–519.
- Böhm, H.P., 1989. A general equation for the terminal fall speed of solid hydrometeors. *J. Atmos. Sci.* 46, 2419–2427.
- Chen, J.P., 1992. Numerical simulation of the redistribution of atmospheric trace chemicals through cloud processes. PhD Thesis. The Pennsylvania State Univ., University Park, PA 16802, 342 pp.
- Clark, T.L., 1974. On modeling nucleation and condensation theory in Eulerian spatial domain. *J. Atmos. Sci.* 31, 2099–2117.
- Cotton, W.R., Tripoli, G.J., Rauber, R.M., Mulvihill, E.A., 1986. Numerical simulations of the effects of varying ice crystal nucleation rates and aggregation processes on orographic snowfall. *J. Clim. Appl. Meteorol.* 25, 1658–1680.
- Eagan, R.C., Hobbs, P.V., Radke, L.F., 1974. Particle emissions for a large Kraft paper mill and their effects on the microstructure of warm clouds. *J. Appl. Meteorol.* 13, 535–552.
- Feingold, G., Tzivion, S., Levin, Z., 1988. The evolution of raindrop spectra: Part I. Stochastic collection and breakup. *J. Atmos. Sci.* 45, 3387–3399.
- Fitzgerald, J.W., 1974. Effect of aerosol composition on cloud droplet size distribution: a numerical study. *J. Atmos. Sci.* 31, 1358–1367.
- Flossmann, A.I., Hall, W.D., Pruppacher, H.R., 1985. A theoretical study of the wet removal of atmospheric pollutants: Part I. The redistribution of aerosol particles captured through nucleation and impaction scavenging by growing cloud drops. *J. Atmos. Sci.* 42, 582–606.
- Hall, W.D., 1980. A detailed microphysical model within a two-dimensional dynamic framework: model description and preliminary results. *J. Atmos. Sci.* 37, 2486–2507.
- Hindman, E.E. II, Hobbs, P.V., Radke, L.F., 1977. Cloud condensation nuclei from a paper mill: Part I. Measured effect on clouds. *J. Appl. Meteorol.* 16, 745–752.
- Hobbs, P.V., Bowdle, D.A., Radke, L.F., 1985. Particles in the lower troposphere over the high plains of the United States: Part I. Size distributions, elemental composition and morphologies. *J. Clim. Appl. Meteorol.* 24, 1344–1356.
- Hudson, J.G., Squires, P., 1976. An improved continuous flow diffusion cloud chamber. *J. Appl. Meteorol.* 15, 776–782.
- Johnson, D.B., 1982. The role of giant and ultragiant aerosol particles in warm rain initiation. *J. Atmos. Sci.* 39, 448–460.
- Kogan, Y.L., 1991. The simulation of a convective cloud in a 3-D model with explicit microphysics: Part I. Model description and sensitivity experiments. *J. Atmos. Sci.* 48, 1160–1189.
- Kuba, N., Takeda, T., 1983. Numerical study of the effect of CCN on the size distribution of cloud droplets: Part II. Formation of large droplets. *J. Meteorol. Soc. Jpn.* 61, 375–387.

- Lew, J.K., Kingsmill, D.E., Montague, D.C., 1985. A theoretical study of the collision efficiency of small planar ice crystals colliding with large supercooled water drops. *J. Atmos. Sci.* 42, 857–862.
- Long, A.B., 1974. Solutions to the droplet coalescence equation for polynomial kernels. *J. Atmos. Sci.* 11, 1040–1057.
- Low, T.B., List, R., 1982a. Collision coalescence and breakup of raindrops: Part I. Experimentally established coalescence efficiencies and fragments size distribution in breakup. *J. Atmos. Sci.* 39, 1591–1606.
- Low, T.B., List, R., 1982b. Collision coalescence and breakup of raindrops: Part II. Parameterization of fragment size distributions in breakup. *J. Atmos. Sci.* 39, 1607–1618.
- Martin, J.J., Wang, P.K., Pruppacher, H.R., 1982. A numerical study of the effect of electric charges on the efficiency with which planar ice crystals collect supercooled cloud drops. *J. Atmos. Sci.* 38, 2462–2469.
- Mather, G.K., 1991. Coalescence enhancement in large multicell storms caused by the emissions from a Kraft paper mill. *J. Appl. Meteorol.* 30, 1134–1146.
- Meyers, M.P., DeMott, P.J., Cotton, W.R., 1992. New primary ice-nucleation parameterizations in an explicit cloud model. *J. Appl. Meteorol.* 31, 708–721.
- Monin, A.C., Yaglom, A.M., 1968. In: *Statistical Hydromechanics*. Izdatel'stvo Nauka, p. 2.
- Mordy, W., 1959. Computation of the growth by condensation of a population of cloud droplets. *Tellus* 11, 16–44.
- Mossop, S.C., 1978. The influence of drop size distribution on the production of secondary ice particles during graupel growth. *Q. J. R. Meteorol. Soc.* 104, 323–330.
- Ochs, H.T., Czys, R.R., Beard, K.V., 1986. Laboratory measurements of coalescence efficiencies for small precipitating drops. *J. Atmos. Sci.* 43, 225–232.
- Orville, H.D., Kopp, F.J., 1977. Numerical simulation of the life history of a hailstorm. *J. Atmos. Sci.* 34, 1596–1618.
- Pruppacher, H.R., Klett, J.D., 1997. *Microphysics of Clouds and Precipitation*. Reidel, 954 pp.
- Radke, L.F., Turner, F.M., 1972. An improved automatic cloud condensation nucleus counter. *J. Appl. Meteorol.* 11, 105–109.
- Rasmussen, R.M., Heymsfield, A.J., 1985. A generalized form for impact velocities used to determine graupel accretional densities. *J. Atmos. Sci.* 42, 2275–2279.
- Rasmussen, R.M., Heymsfield, A.J., 1987. Melting and shedding of graupel and hail: Part I. Model physics. *J. Atmos. Sci.* 44, 2754–2763.
- Reisin, T., Levin, Z., Tzivion, S., 1996a. Rain production in convective clouds as simulated in an axisymmetric model with detailed microphysics: Part II. Effects of varying drops and ice initiation. *J. Atmos. Sci.* 53, 1815–1837.
- Reisin, T., Levin, Z., Tzivion, S., 1996b. Rain production in convective clouds as simulated in an axisymmetric model with detailed microphysics: Part I. Description of the model. *J. Atmos. Sci.* 53, 497–519.
- Reisin, T., Tzivion, S., Levin, Z., 1992. The influence of warm microphysical processes on ice formation and diffusional growth — a numerical study. In: 11th Int. Conf. Clouds Precip., Montreal, Canada, 17–21 August. pp. 280–283.
- Respondek, P.S., Flossmann, A.I., Alheit, R.R., Pruppacher, H.R., 1995. A theoretical study of the wet removal of atmospheric pollutants: Part V. The uptake, redistribution, and deposition of  $(\text{NH}_4)_2\text{SO}_4$  by a convective cloud containing ice. *J. Atmos. Sci.* 52, 2121–2132.
- Smolarkiewicz, P.K., 1983. A simple positive definite advection scheme with small implicit diffusion. *Mon. Weather Rev.* 111, 479–486.
- Takahashi, T., 1976. Warm rain, giant nuclei and chemical balance — a numerical model. *J. Atmos. Sci.* 33, 269–286.
- Takahashi, T., Lee, S., 1978. The nuclei mass range most efficient for the initiation of warm cloud showers. *J. Atmos. Sci.* 35, 1934–1946.
- Takeda, T., Kuba, N., 1982. Numerical study of the effect of CCN on the size distribution of cloud droplets: Part I. Cloud droplets in the stage of condensation growth. *J. Meteorol. Soc. Jpn.* 60, 978–993.
- Twomey, S., 1963. Measurements of natural cloud nuclei. *J. Rech. Atmos.* 1, 101–105.
- Tzivion, S., Feingold, G., Levin, Z., 1987. An efficient numerical solution to the stochastic collection equation. *J. Atmos. Sci.* 44, 3139–3149.

- Tzivion, S., Feingold, G., Levin, Z., 1989. The evolution of raindrop spectra: Part II. Collisional collection/breakup and evaporation in a rainshaft. *J. Atmos. Sci.* 46, 3312–3327.
- Tzivion, S., Reisin, T., Levin, Z., 1994. Numerical simulation of hygroscopic seeding in a convective cloud. *J. Appl. Meteorol.* 33, 252–267.
- Wang, C., Chang, J.S., 1993. A three-dimensional numerical model of cloud dynamics, microphysics, and chemistry: Part I. Concepts and formulation. *J. Geophys. Res.* 98, 14827–14844.
- Woodcock, A.H., Duce, R.A., Moyers, J.L., 1971. Salt particles and raindrops in Hawaii. *J. Atmos. Sci.* 28, 1252–1257.